Combustion synthesis and characterization of Cu–Sm co-doped CeO$_2$ electrolytes

Yingchao Dong [a,*], Stuart Hampshire [a,*], Jian-er Zhou [b], Xinfa Dong [d], Bin Lin [c], Guangyao Meng [c]

[a] *Materials and Surface Science Institute (MSSI), University of Limerick (UL), Ireland*
[b] *Key Lab of Jiangxi Universities for Inorganic Membranes, Jingdezhen Ceramic University, China*
[c] *USTC Lab for Solid State Chemistry and Inorganic Membranes, University of Science and Technology of China (USTC), China*
[d] *School of Chemistry and Chemical Engineering, South China University of Technology (SCUT), China*

Abstract

Nano-sized CSO (Ce$_{0.80}$Sm$_{0.20}$O$_{2-\delta}$) and CSCO (Ce$_{0.79}$Sm$_{0.20}$Cu$_{0.01}$O$_{2-\delta}$) were synthesized by the PVA assisted combustion method, and then characterized by the structure of PVA–cation complexes and nano-powders, as well as mechanical and electrical performance after sintering. The results indicate that the PVA–cation complexes (PVA–(Ce^{3+},Sm^{3+}) and PVA–(Ce^{3+},Sm^{3+},Cu^{2+})) were formed by coordinating metal cations to hydroxyl groups, as well as the COO^{-1} group derived from the oxidation of PVA with NO$_3$$^{-1}$. Low temperatures (around 200 °C) caused intense combustion reactions, resulting in the direct crystallization of cubic fluorite nano-CSO (10–20 nm) and nano-CSCO (10–15 nm) crystals with homogeneous element distribution. This slight compositional modification of CSO by co-doping with 1 mol% CuO resulted in a significantly lowered densification temperature, as well as enhanced mechanical and electrical property. The strength improvement can be ascribed to the dense and fine-grained microstructure without normal grain coarsening, resulting in a transgranular-dominant fracture mode during strength testing.

1. Introduction

In the past decades, CeO$_2$-based materials doped with rare earth elements (Gd^{3+}, Sm^{3+}, Y^{3+}, Nd^{3+} and La^{3+}) have been widely studied as promoter for heterogeneous catalytic reaction and electrolyte for solid oxide fuel cells (SOFCs).[1–5] Among them, Sm-doped CeO$_2$ is being developed as a viable alternative to yttria-stabilized zirconia (YSZ) as solid electrolyte for intermediate and low temperature SOFC applications, owing to high oxygen-ionic conductivity, good chemical compatibility with electrodes and low operating temperature.[1] Moreover, the Sm^{3+} doping has the smallest association enthalpy between dopant cations and oxygen vacancies in the cubic fluorite lattice. It is well verified that high electrical conductivity can be achieved

for 20 mol% Sm-doped ceria, i.e., Ce$_{0.8}$Sm$_{0.2}$O$_{2-\delta}$ (CSO).[2,3] However, it is still difficult for CSO electrolytes to be sintered to high densities below 1500 °C for the conventional synthesis method, i.e., the solid state reaction of CeO$_2$ and Sm$_2$O$_3$.[2] High sintering temperatures are disadvantageous for fabrication of SOFCs because ceria-based electrolytes and electrodes cannot be co-fired at temperatures higher than 1300 °C, especially for cathode-supported SOFCs.[3] Also, high temperature sintering leads to the partial reduction from Ce^{4+} to Ce^{3+} in the ceria-based materials above 1200 °C, especially at low oxygen partial pressures.

In order to prepare a dense CeO$_2$-based electrolyte at reduced densification temperature, several effective methods have been developed such as addition of low melting-point sintering aids[4,5] and adoption of high sintering activity nano-sized powders synthesized by various wet chemical techniques such as sol–gel,[6] citrate–nitrate process,[7] hydrothermal synthesis,[2] co-precipitation,[8] etc. The products derived from these wet-chemical methods usually show better performance due to their higher homogeneity in composition. However, the traditional

* Corresponding authors. Tel.: +353 61202640; fax: +353 61338172.
E-mail addresses: yingchao.dong@ul.ie, dongyc9@mail.ustc.edu.cn (Y. Dong), Stuart.Hampshire@ul.ie (S. Hampshire).

wet-chemical synthesis is complicated and time-consuming, such as in the sol–gel process.

Recently, interest has actively focused on polymer assisted combustion synthesis, which can produce high-quality nano-sized powders with high specific surface area, homogeneous microstructure and fewer impurities at very low temperatures.[9,10] More especially, this technique shows several advantages in the synthesis of multi-component compound powders, allowing dopant incorporation into the lattice during instant combustion and avoiding deviations from stoichiometry. As a low-cost organic fuel, polyvinyl alcohol (PVA) with isolated hydroxyl functional groups can not only adsorb but also complex with metal cations. In aqueous solution, PVA can induce the homogeneous incorporation of metal cations into its polymer network structure and prevent their flocculation or precipitation. In recent years, PVA has been successfully used in the synthesis of high-quality nano-sized powders such as pure oxides including Co_3O_4,[11] Nd_2O_3,[12] and multi-compositional oxides including cordierite ($2MgO\cdot2Al_2O_3\cdot5SiO_2$),[13] $CaAl_2O_4$, $Y_4Al_2O_9$, YPO_4,[14,15] $Ca_4Al_6O_{16}S$,[16] $LiMn_2O_4$,[17] $Ce_{0.8}Gd_{0.2}O_{2-\delta}$[18] and Cr-stabilized ZrO_2.[19] However, little research has been reported on the synthesis of CSO-based electrolyte powders by this simple PVA assisted combustion process. Nano-crystalline CSO powder was firstly prepared with PVA as fuel and reductant.[20] Nevertheless, in order to achieve high densities, it is still necessary to sinter this CSO at relatively high temperatures (1300 °C).

Doping with CuO is effective in lowering the sintering temperature of (1) Gd-doped $BaCeO_3$ (by ~150 °C) with higher conductivity in both air and hydrogen atmospheres,[21] (2) 10 mol% Gd-doped CeO_2 without much loss of electrical conductivity,[22] and (3) Y-doped $BaZrO_3$.[23] In previous work,[24] a Cu-doped gadolinium-ceria electrolyte, $Ce_{0.79}Gd_{0.20}Cu_{0.01}O_{2-\delta}$ (CGCO) with fluorite structure, was synthesized by combustion reaction method with PVA, producing fine nano-crystals of CGCO ranging from 30 to 50 nm. This was sintered at a temperature as low as 1100 °C, exhibiting a dense fine-grained microstructure and possessing remarkably improved electrical conductivity of 0.026 S cm^{-1} at 600 °C and ambient three-point flexural strength of 148 ± 2.4 MPa. The sintering temperature is very close to the processing temperature of cathode components which offers the possibility of co-sintering for fabrication of cathode-supported SOFCs.

In the current work, a high sintering activity nano-sized $Ce_{0.79}Sm_{0.20}Cu_{0.01}O_{2-\delta}$ (CSCO) powder was synthesized by the PVA assisted combustion method and doped with 1 mol% CuO. The un-doped CSO powder was synthesized by the same method for comparison. The transformation behaviour of cation–PVA complexes into ceramic powders, crystalline structure and morphology have been characterized by TG-DSC (Thermo-Gravimetric and Differential Scanning Calorimetry), FT-IR (Fourier Transform Infrared Spectrometry), XRD (X-ray Diffraction), FESEM (Field Emission Scanning Electronic Microscopy) and HRTEM (High-Resolution Transmission Electron Microscopy). In addition, the densification during sintering, the mechanical properties and fracture mechanisms, and con-

ductivity are preliminarily compared for possible application as SOFC electrolyte.

2. Experimental

2.1. Synthesis of nano-sized CSO and CSCO powders

Both nano-sized CSO and CSCO powders were synthesized by the PVA combustion method. Firstly, the mixed solution with a concentration of 0.5 M cations was obtained by dissolving $Ce(NO_3)_3\cdot6H_2O$ (≥99.0%; Sinopharm Chemical Reagent Co., Ltd.), $Cu(NO_3)_2\cdot3H_2O$ (≥99+% for analysis; Acros Organics) and Sm_2O_3 (3 N, 99.9%; Sinopharm Chemical Reagent Co., Ltd.) with correct stoichiometric proportions in distilled water and dilute nitric acid, respectively. Subsequently, the 5.00 wt.% aqueous PVA solution (typical MW 89,000–98,000, 99+% hydrolyzed; Aldrich Chemical Company) was added to the mixed metal cation nitrate solution with the molar ratio (PVA monomer to total cation) of 2:1. Afterwards, the mixed solution was homogenized at 90 °C for 12 h to vaporize excessive water, and then transferred into a 1000 ml ceramic basin on a hot plate. After a while, the combustion reaction took place dramatically in an instant, accompanied by a slight sound of explosion. Afterwards, the as-synthesized powders were calcined at 600 °C for 2 h.

2.2. Attrition milling, dry-pressing and sintering

The as-calcined CSO and CSCO powders were attrition-milled respectively in distilled water for 2 h at an attrition speed of 500 rpm min^{-1}, then shell frozen sufficiently at temperatures lower than −18 °C, and retrieved subsequently using a vacuum freeze dryer for three days. With PVA-1750 solution (5.00 wt.%) as organic binder, small CSO and CSCO pellets (ϕ 20 mm) were uniaxially pressed using a hydraulic press machine at a pressure of 490 MPa.

After drying at 80 °C for 24 h, the CSCO disc samples were sintered in air for 5 h at 900–1100 °C, while the CSO samples were sintered in air for 5 h at 1200–1400 °C at intervals of 50 °C. For all samples, two temperature-dependent heating rates of 2 °C min^{-1} and 3 °C min^{-1} were applied for temperatures lower and higher, respectively, than 500 °C. A holding time of 1 h was performed at 500 °C in order to remove organic binder added.

2.3. Characterization

Both CSO and CSCO samples, each including dried gel and synthesized powder, were analyzed by TG-DSC (SDT Q600, The M&P Lab, USA) from room temperature to 900 °C and 1000 °C at a constant heating rate of 5 °C min^{-1}. FT-IR spectroscopy (Spectrum 2000, PerkinElmer, USA) was carried out to investigate the structure of the PVA–(Ce^{3+},Sm^{3+}) and PVA–(Ce^{3+},Sm^{3+},Cu^{2+}) using the potassium bromide (KBr) pellet technique.

Both CSO and CSCO samples, each including dried gel, synthesized powder and calcined powder, were directly characterized using XRD (Cu Kα radiation; Philips X' Pert MPD Pro

diffractometer, Philips, The Netherlands). Scans ranged from $10° < 2\theta < 80°$ with a step size of $0.25°$ and a time per step of 20 s.

HR-TEM (JEM-2010, JEOL, Japan) was employed to characterize CSO and CSCO nano-crystals for the as-synthesized and calcined powders. SEM (SU70 FE-SEM, Hitachi High-Technologies Europe GmbH, Krefeld, Germany) and EDS (INCA300, Oxford Instrument, England) micro-region compositional analysis were carried out on CSO and CSCO samples.

The bulk densities of the CSO and CSCO sintered bodies were measured in distilled water using a conventional method according to the Archimedes' principle. The relative density of a sample was calculated using the relation $\%\ \text{density} = (d_m/d_{th}) \times 100$, where, d_m is the bulk density measured by the Archimedes replacement method and d_{th} is the theoretical density given by the following two equations for CSO and CSCO solid solutions:

$$d_{th,CSO} = \frac{4}{N_A a^3} \left((1-x)M_{Ce} + xM_{Sm} + \left(2 - \frac{x}{2}\right) M_O \right) \quad (1)$$

$$d_{th,CSCO} = \frac{4}{N_A a^3} ((1 - (x-y))M_{Ce} + xM_{Sm}$$
$$+ yM_{Cu} + \left(2 - \frac{x}{2}\right) M_O \Big) \quad (2)$$

where x is Sm content ($x = 0.2$), y is copper content ($y = 0.01$), a is the lattice constant at room temperature (for CSO $a = 0.54279$ nm and for CSCO $a = 0.54253$ nm), N_A is the Avogadro number (6.022×10^{23}), and M refers to the atomic weight.

Biaxial flexural strength (BFS) tests were performed according to standard procedures.[25,26] Seven disc specimens (diameters: 15–17 mm; thicknesses: 0.7–0.85 mm) for one set were prepared. A load frame (Lloyd LR50K, UK) with a crosshead speed of $0.1\ \text{mm min}^{-1}$ and a preload of 2 N was utilised along with a test jig with a support radius of 4.1 mm. In order to understand the fracture mechanisms, SEM observations were performed on the surfaces, as well as the fracture surfaces of CSO (1400 °C) and CSCO (950 °C) generated as a result of the flexural strength test.

Vickers hardness tests were performed using a diamond indentation technique.[26] All the samples were polished by 240-mesh, then 400-mesh metallographic sandpapers, followed by CeO_2 polishing paste (1 μm). The resultant indents ($n = 10$ per composition, across 3 different samples) were measured under a 200–300 N load for 10 s. Thermal expansion co-efficient (TEC) was measured between room temperature (26 °C) and 1000 °C in a horizontal dilatometer (DIL 402C, Netzsch, Germany). A constant heating rate of $10\ °\text{C min}^{-1}$ was used.

AC impedance spectroscopy measurements were conducted on electrochemical impedance spectrum analyzer (CHI 600A, Chenhua Inc., Shanghai, PR China) in the frequency range of 0.1–100 kHz. The pellets were coated with silver paste followed by firing at 800 °C for 1 h before tests, then put into the tube furnace and heated at a heating rate of $2\ °\text{C min}^{-1}$ in air. Measurements were made between 400 and 800 °C at intervals of 50 °C. In all measurements, the lead resistance was subtracted by measuring the impedance of a blank cell. The conductivity

values at different temperatures were calculated according to the following equation:

$$\sigma = \frac{L}{RS} \quad (3)$$

where L is the thickness of the tested pellets, S the effective area of the pellets ($S = 0.25\pi D^2$, D is diameter) and R the resistance at different temperatures.

Raman spectra were obtained by using a JY-HR800 spectrometer with a He–Ne ion laser. The excitation wave number is 632.8 nm with a resolution of $1\ \text{cm}^{-1}$.

3. Results and discussion

3.1. TG-DSC analysis

Fig. 1 shows the thermal evolution behaviour of the CSO and CSCO dried gels, and synthesized powders investigated by TG-DSC analysis under air. For CSO dried gel (Fig. 1a), there is an endothermic DSC peak at 68.1 °C with a mass loss of 14.00 wt.% between 26 and 190 °C, which was caused by the removal of physically adsorbed water and polymer condensation reactions within the precursors. A very sharp exothermic peak at 202 °C on the DSC curve suggests that an intensive combustion reaction occurred, which is slightly lower than the initiation temperature of 220 °C for $Ce_{0.8}Gd_{0.2}O_{2-\delta}$ synthesis.[18] It should be noted that the weight loss reaches almost 100% on the TG curve because the powder was removed from the Pt crucible due to the instantaneous release of a large quantity of gases during the combustion process. For the synthesized CSO powder (Fig. 1b), the physically adsorbed water was removed at 67.1 °C, associated with a slight mass loss of 1.69 wt.%. No further reaction is observed until a small exothermic DSC peak at 902 °C, indicating the further combustion of residual carbon in the synthesized powder. The corresponding weight loss is as low as 1.28%.

Similar thermal evolution behaviour is observed for the CSCO dried gel and synthesized powder (Fig. 1c and d). For CSCO gel, the redox combustion reaction between PVA and metal nitrates was initiated at very low temperature of about 200.6 °C. After combustion reaction, residual carbon was burned out at 892.9 °C along with a very low mass loss of 2.41%.

3.2. FT-IR analysis

Fig. 2 shows the FTIR spectra of "pure" PVA, the precursors (PVA–cation complexes) and the as-synthesized and calcined powders of the CSO- and CSCO-based materials. The precursors of both CSO and CSCO exhibit similar FT-IR spectra, as do the as-synthesized and calcined forms of each material. By comparing the spectra of pure PVA, with CSO- and CSCO-based PVA–cation complexes, significant changes in the spectra at 1000–1700 and 2500–3000 cm^{-1} can be analyzed. The following explanations can be made: Absorption peaks around 3450–3460 cm^{-1} can be assigned to the stretching vibration of hydrogen-bonded OH groups. Absorption peaks of 2909 and 2951 cm^{-1} can be assigned to the stretching vibration of the CH_2 group. Absorption peaks around 1635 cm^{-1} can be
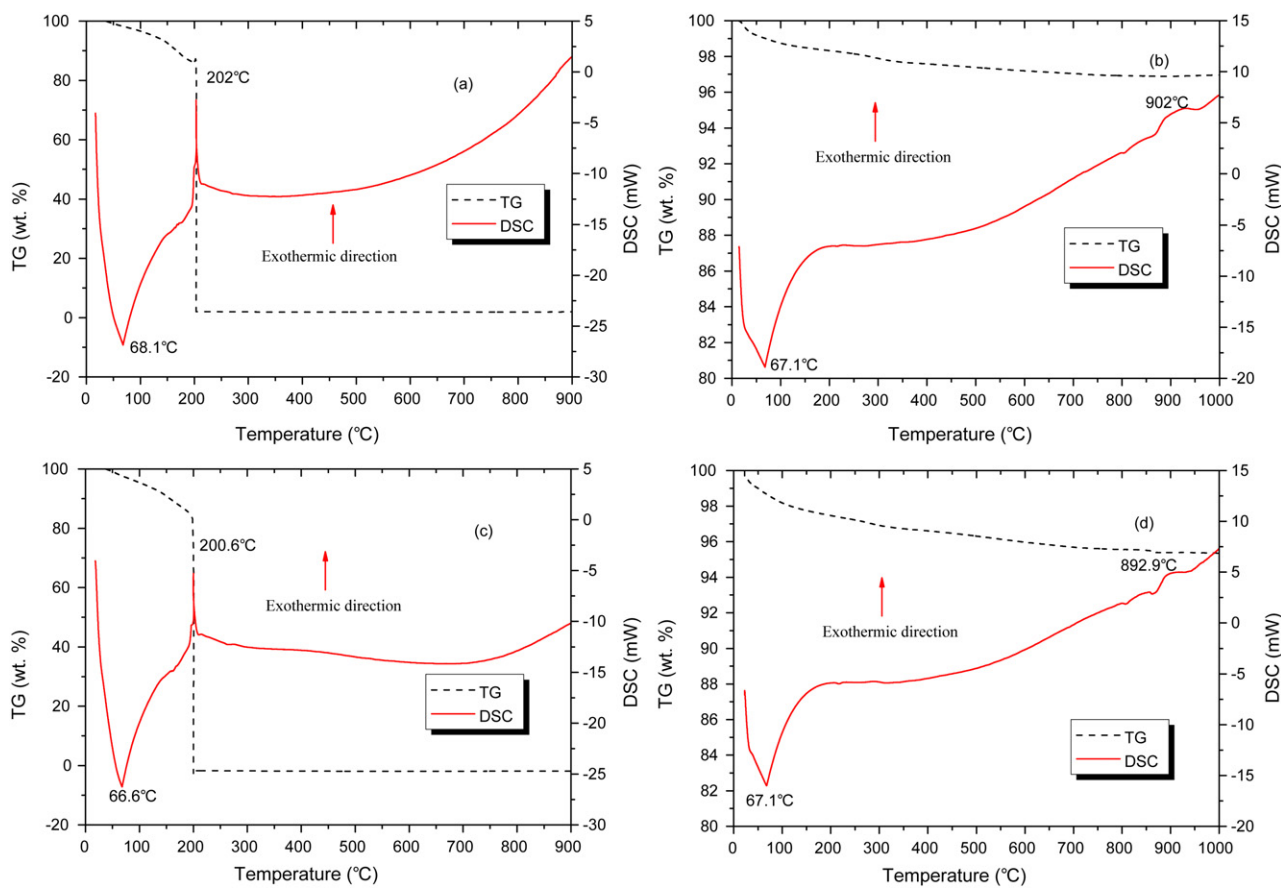
Fig. 1. TG-DSC curves of the CSO and CSCO-based materials: (a) CSO dried gel; (b) as-synthesized CSO; (c). CSCO dried gel; (d) as-synthesized CSCO.

assigned to the asymmetric stretching vibration of the COO^{-1} group. This is not observed in the PVA spectrum. It is concluded that the COO^{-1} groups in the PVA–cation complexes (PVA–(Ce^{3+},Sm^{3+}) and PVA–(Ce^{3+},Sm^{3+},Cu^{2+})) are formed by the oxidation of the PVA with the NO_3^{-1} ion as a strong oxidizing agent. Absorption peaks at $1440\,cm^{-1}$ and $1100\,cm^{-1}$ can be assigned to the angular vibration of the CH_2 group and the stretching vibration of CH_3, respectively.[15] Compared with pure PVA, no peaks at 2909 and $2951\,cm^{-1}$ can be found in CSO and CSCO-based PVA–cation complexes, associated with the decrease in peak intensity around $1440\,cm^{-1}$ and $1100\,cm^{-1}$ indicating again the formation of COO^{-1} groups due to the degradation of PVA. The shift in the adsorption peak of the COO^{-1} group from 1651 to $1635\,cm^{-1}$ indicates that some cations are chelated by the carboxylic group. The hydroxyl oxygen is coordinated by metal cations, which is suggested by the shift of OH peak from 3432 to $3460\,cm^{-1}$. Also, the decrease in adsorption peak intensity of OH group at 3000–$3800\,cm^{-1}$ suggests that some hydroxyl bonds are cleaved during the formation of PVA–cation complexes. Therefore, it is concluded that the cations are trapped in the structure of PVA in two ways: (1) coordination to the COO^{-1} group or (2) coordination to the hydroxyl group. This therefore results in a homogeneous distribution of metal cations at an atomic scale in the network of the dried polymer carrier during the process. In the PVA solution process, a homogeneously mixed solution was easily obtained

by completely dissolving as-required metal nitrates without any adjustment of solution pH, compared with the mixed sol–gel processing route.[18–20]

By comparison, both as-synthesized and calcined CSO and CSCO powders have no hydroxyl groups, except for the OH species from the adsorbed moisture, which suggests that the combustion reaction was complete with removal of most of the organic species except that some COO^{-1} ions (at $1635\,cm^{-1}$) remain in the as-synthesized materials. The absorption band at $1382\,cm^{-1}$ which is usually associated with C-O bond stretching in inorganic carbonates[15] is almost absent in the as-synthesized materials and not present in the calcined materials. By comparing the FT-IR spectra of the as-synthesized CSO and CSCO, with the as-calcined CSO and CSCO, there are still several low intensity bands related to physically adsorbed water, residual nitrate ion, and that assigned to the Ce–O bond (around $480\,cm^{-1}$).

3.3. XRD pattern

Fig. 3 shows the XRD patterns of the CSO and CSCO samples, each including the dried gels, the as-synthesized powders, and the calcined powders. It can be seen from Fig. 3a and b that both the CSO-based and CSCO-based polymer gels are amorphous to X-rays, suggesting again that all metal cations are physically entrapped and then chemically bound with hydroxyl and COO^- functional groups in large chain molecule PVA. It is
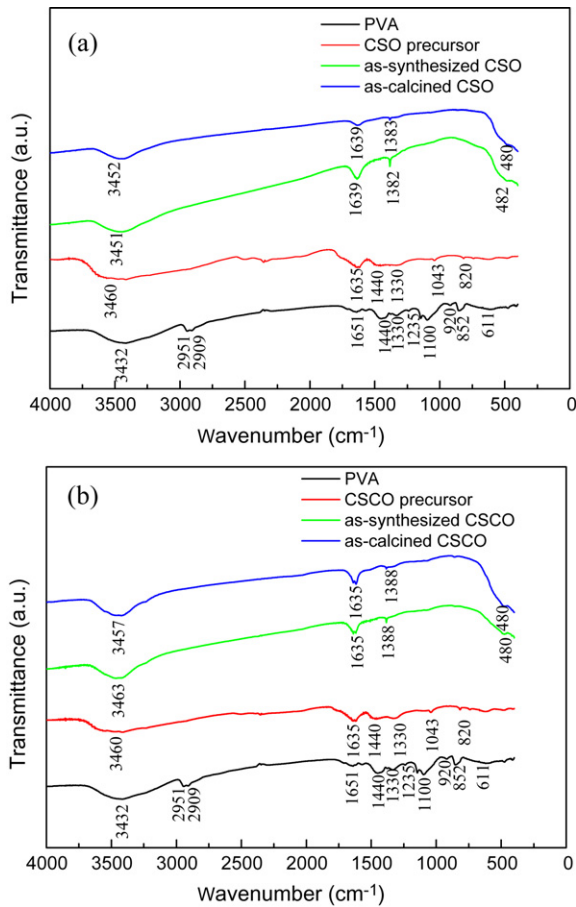
Fig. 2. FT-IR spectra of (a) CSO-based materials and (b) CSCO-based materials.

seen from Fig. 3c and d that both CSO and CSCO powders after combustion reaction are crystalline in nature with cubic fluorite structure (CeO_2). The diffraction peaks could be indexed according to a pure cubic phase (*Fm3m* space group) of CeO_2.
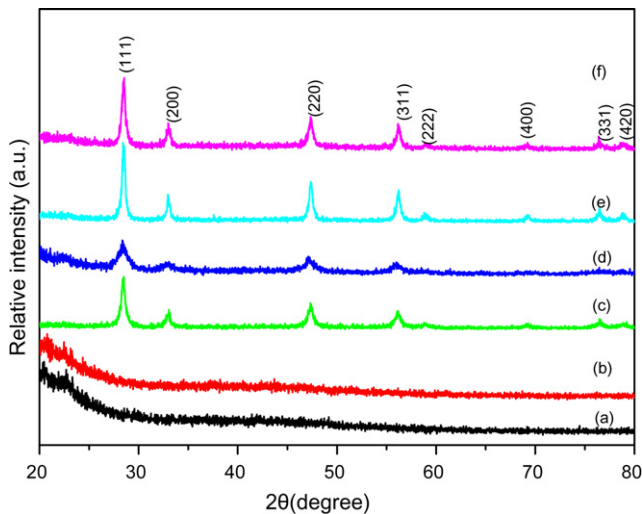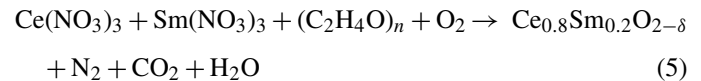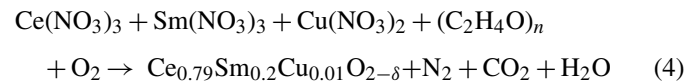

Fig. 3. XRD patterns of the CSO and CSCO-based materials: (a) dried CSO gel; (b) dried CSCO gel; (c) as-synthesized CSO powder; (d) as-synthesized CSCO powder; (e) calcined CSO powder at 600 °C for 2 h; and (f) calcined CSCO powder at 600 °C for 2 h.

No Sm_2O_3 phase is observed, indicating the formation of single-phase solid solution via the direct dissolution of Sm_2O_3 into the lattice of CeO_2 during combustion process. This is similar to the PVA processed Gd-substituted CeO_2 (CGO),[18,24] but different from the amorphous state of PVA combustion processed cordierite,[13] $Ca_4Al_6O_{16}S$,[16] $CaAl_2O_4$ and YAG,[15] which needed further calcination for crystallization. In our case, as shown in Fig. 1a and c, a large quantity of reaction heat was released, which resulted in a relatively high temperature for the reaction over a very short time, which was enough to cause the crystallization of nano-sized CSO and CSCO. Also, by comparing Fig. 3c with d, it appears that the addition of a minor amount of CuO has no effect on the crystal structure, except for a slight decrease in peak intensity, which is opposite to the increase of peak intensity for the hydrothermally processed Cu-doped CeO_2 nano-powder.[27] In our case, this is because there is a lower content of nitrate in CSCO for the same molar amount of CSO and CSCO, resulting in lower values of combustion heat, which is in good agreement with the observations of weaker exothermic peaks on the DSC curves of the CSO and CSCO dried gels (see Fig. 1a and c). The combustion reaction equations between metal nitrates and PVA can be summarised as follows:

$$Ce(NO_3)_3 + Sm(NO_3)_3 + Cu(NO_3)_2 + (C_2H_4O)_n$$
$$+ O_2 \rightarrow Ce_{0.79}Sm_{0.2}Cu_{0.01}O_{2-\delta} + N_2 + CO_2 + H_2O \quad (4)$$

$$Ce(NO_3)_3 + Sm(NO_3)_3 + (C_2H_4O)_n + O_2 \rightarrow Ce_{0.8}Sm_{0.2}O_{2-\delta}$$
$$+ N_2 + CO_2 + H_2O \quad (5)$$

After calcination at 600 °C, the crystalline phases of the CSO and CSCO powders were well developed, which is confirmed by the sharp diffraction peaks in the XRD patterns (Fig. 3e and f). The crystalline unit cell parameters of the calcined CSO and CSCO were also calculated. The cell parameter and cell volume of the calcined CSCO powder is 0.54253 nm and 1.56909 nm^3, which is a little lower than for the CSO ($a = 0.54279$ nm; cell volume = 1.599217 nm^3). Such a decrease is probably due to the substitution of smaller Cu^{2+} ions ($r = 0.073$ nm) for Ce^{4+} ions ($r = 0.097$ nm) in the cubic lattice of the CSO structure.[28]

3.4. TEM and SEM-EDS

Fig. 4 presents the TEM micrographs of the as-synthesized CSO powder. From Fig. 4a, it can be seen that a porous agglomerated microstructure has evolved as a result of the gases instantly released by the intense redox reaction of PVA and metal nitrates under fuel-rich conditions. PVA networks not only acted as fuel and reductant, but also maintained their pore structures. This highly porous structure is quite typical for nano-sized powders prepared by the polymer-assisted combustion technique.[11–20] Fig. 4b clearly shows the formation of CSO nano-sized crystals with uniform size and agglomerated compact state. Most of the CSO crystals have a size range of 10–20 nm. The observed CSO crystals compact with each other, which is due to strong agglomeration during combustion process. The HRTEM image (Fig. 4c)
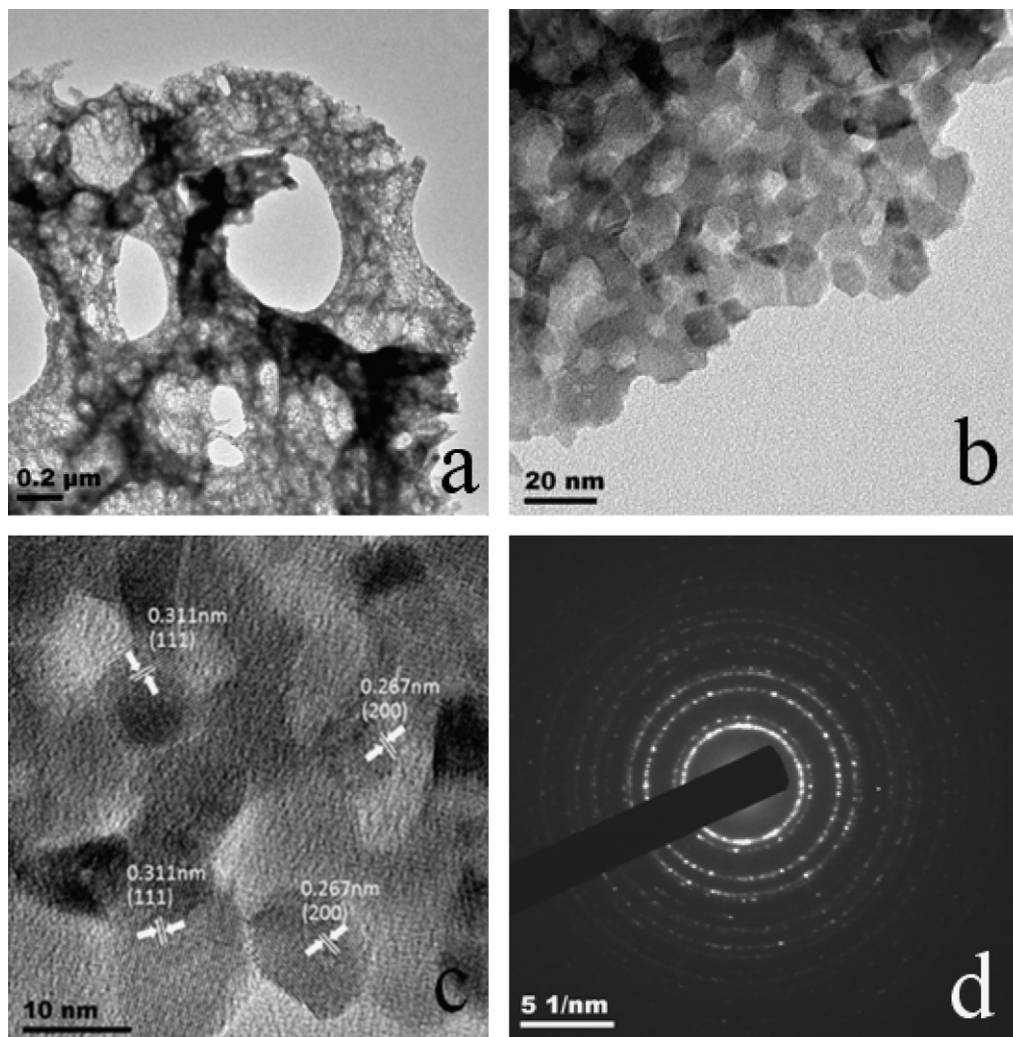
Fig. 4. TEM micrographs of the as-synthesized CSO powders without any treatments: (a) low magnification; (b) high magnification; (c) HRTEM; (d) SAED pattern.

shows nano-crystals with lattice planes with d-spacings of about 0.311 and 0.267 nm, which can be assigned to the (1 1 1) and (2 0 0) planes of CSO with cubic fluorite structure. This further confirms that nano-sized CSO crystals were directly formed by this simple PVA combustion technique. The selected area electron diffraction (SAED) pattern in Fig. 4d, exhibits eight broad rings which can be attributed to (1 1 1), (2 0 0), (2 2 0), (3 1 1), (2 2 2), (4 0 0), (3 3 1) and (4 2 0) reflections of fcc CSO.

Fig. 5 shows TEM micrographs of the as-synthesized CSCO powder. While the morphology of CSCO is similar to that of CSO, nevertheless, the CSCO shows a relatively poor crystallinity with small crystal size, which is consistent with the TG-DSC and XRD analysis (Sections 3.1 and 3.3). Most of the CSCO crystals have a size range of 10–15 nm and using HRTEM, lattice spacings could be determined and these were found to be the same as for CSO. SAED once again confirmed the cubic fluorite structure for this compound. Following the polymer assisted combustion experiments, the as-synthesized CSO and CSCO were quite friable due to their sponge-like structure.

To study the element distribution of the multi-compositional CSCO powder, SEM-EDS analysis was performed on the as-synthesized CSCO (Fig. 6). Fig. 6a clearly shows the high volume fraction of non-uniform porosity with sponge-like structure found in the as-synthesized CSCO. From Fig. 6b–d, it is noted that three elements, including Ce, Sm and Cu, distribute quite homogeneously in the sponge-like CSCO after combustion reaction. This indicates that metal cations were complexed by the hydroxyl and COO^{-1} groups of PVA and then homogeneously distributed in its network structure, without disproportionation from the desired stoichiometry. Fig. 6e shows an EDS spectrum of the whole area in Fig. 6a, which exhibits high peak intensities for Ce and Sm but a very low peak intensity for Cu.

Fig. 7 shows the SEM and TEM images of the CSO and CSCO powders after calcination at 600 °C for 2 h. Both CSO and CSCO agglomerates exhibit a highly porous foam microstructure (Fig. 7a and d). The agglomerates were easily broken up into micron-sized particles after attrition-milling (Fig. 7b and e), which consist of gas cavities and agglomerated fine CSO and CSCO crystals. Most of the CSO and CSCO crystals have a size range of 30–50 nm (Fig. 7c and f), indicating that both CSO and CSCO nano-crystals coarsen after calcination. This is in agreement with the XRD analysis (Section 3.3).
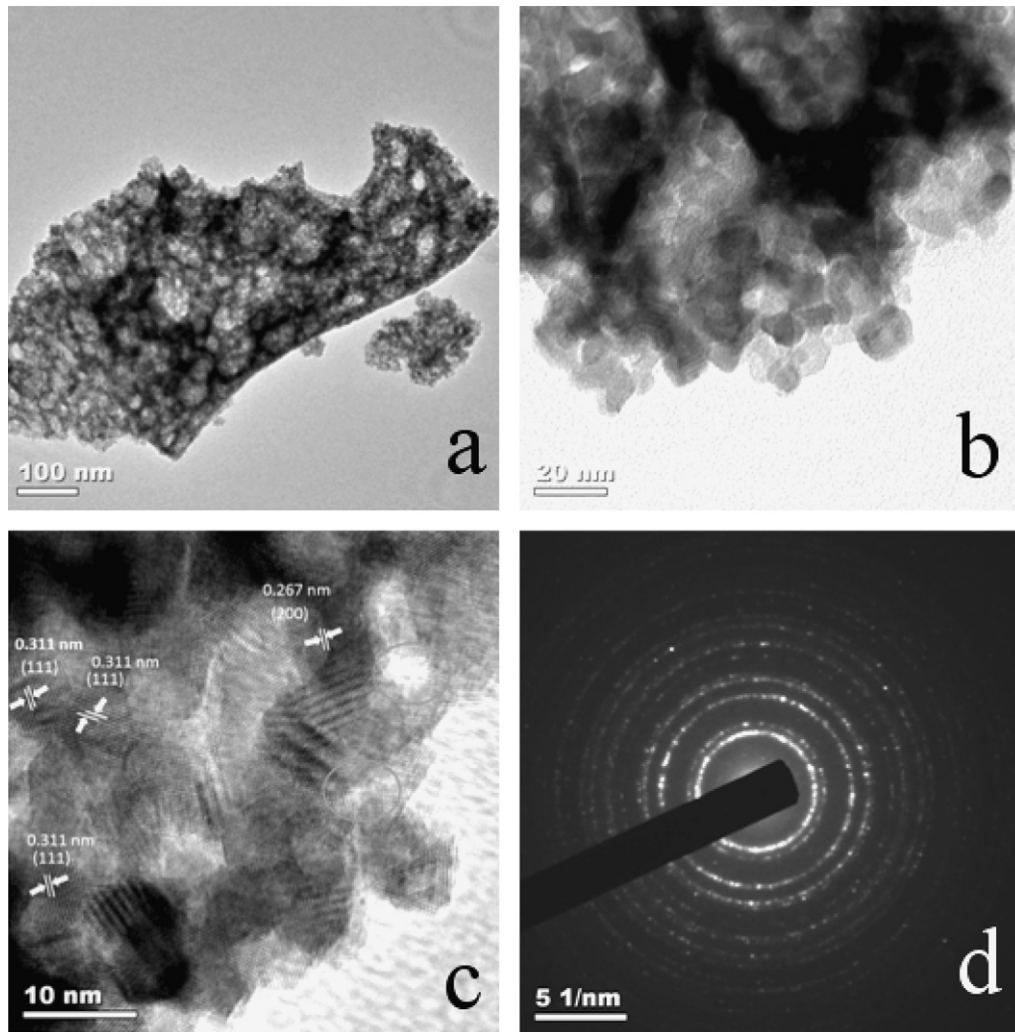
Fig. 5. TEM micrographs of the as-synthesized CSCO powders without any treatments: (a) low magnification; (b) high magnification; (c) HRTEM; (d) SAED pattern.

3.5. Characterization of sintered CSO and CSCO bodies

3.5.1. Sintering of CSO and CSCO

Fig. 8 presents the relative densities of the CSO compacts sintered at 1200–1400 °C, and CSCO compacts sintered at 900–1100 °C. For CSO, a large increase in relative density from $76.0 \pm 2.3\%$ to $93.0 \pm 1.4\%$ is observed as the temperature increases from 1200 °C to 1300 °C, indicating a significant densification process. Above 1300 °C, the relative density increases slightly with sintering temperature. At 1400 °C, a maximum relative density of $96.7 \pm 1.6\%$ is reached. Compared with CSO, the CSCO exhibits a very high sintering activity such that densification was achieved at much lower temperatures. The densification of CSCO mainly took place below 950 °C and, on sintering at 950 °C, it had already attained a high level of relative

density, i.e. $97.2 \pm 0.5\%$, which is higher than that of the CSO (96.7%) sintered at 1400 °C. This significant reduction of 450 °C in densification temperature is ascribed to the effect of doping with 1 at.% CuO. Above 950 °C, the relative density increases slightly with temperature. The relative densities are $97.6 \pm 0.6\%$ at 1000 °C, $98.5 \pm 1.2\%$ at 1050 °C and $98.6 \pm 1.5\%$ at 1100 °C.

In view of their similar relative densities of greater than 96%, the CSO sintered at 1400 °C (CSO-1400) and the CSCO sintered at 950 °C (CSCO-950) were investigated further to compare their microstructure, electrical conductivity, thermal and mechanical properties. Table 1 presents relative density, % volume shrinkage, open porosity and mechanical and thermal properties of CSO-1400 and CSCO-950. The CSCO-950 shows higher shrinkage of $21.8 \pm 0.1\%$ compared with the CSO-1400 ($20.5 \pm 0.4\%$), due to the enhanced sintering as a result of a

Table 1
Shrinkage percents, relative densities, mechanical and thermal properties of the CSO sintered at 1400 °C for 5 h (CSO-1400) and CSCO compacts sintered at 950 °C for 5 h (CSCO-950).

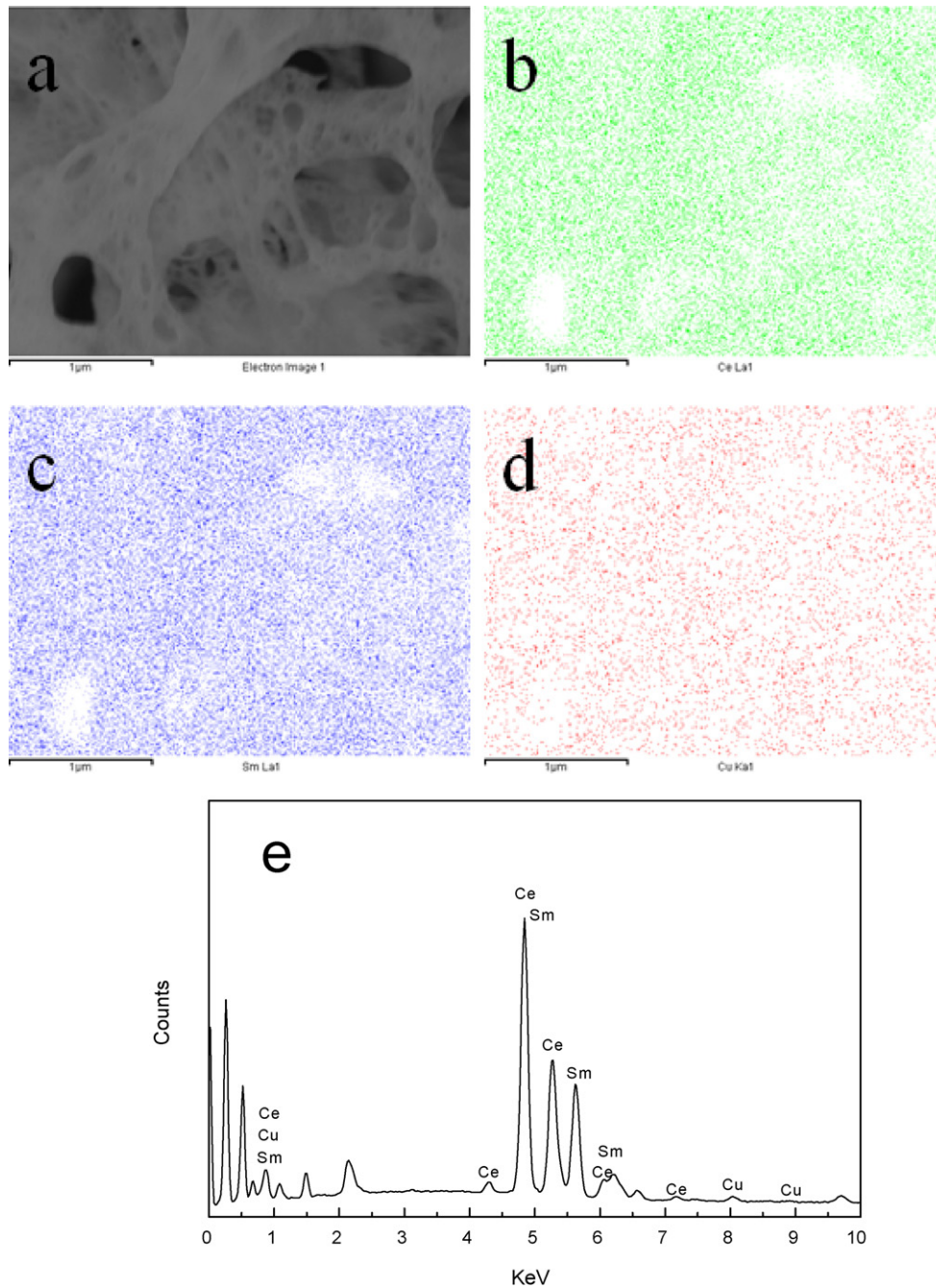| Sample	Relative density (%)	Shrinkage (%)	Open porosity (%)	BFS (MPa)	FEPV (KJ m^{-3})	Hardness (GPa)	TEC ($\times 10^{-6}$ °C^{-1})
CSO-1400	96.7 ± 1.6	20.5 ± 0.4	0	194.4 ± 57.0	53.7 ± 22.0	10.7 ± 0.6	12.83
CSCO-950	97.2 ± 0.5	21.8 ± 0.1	0.6 ± 0.2	257.5 ± 27.4	74.8 ± 17.1	10.5 ± 0.5	12.72

Fig. 6. The SEM-EDS results for the as-synthesized porous CSCO aggregates: (a) SEM micrograph with high magnification; (b) Ce element mapping; (c) Sm element mapping; (d) Cu element mapping; (e) EDS spectrum of the whole area in (a).

very small amount of CuO doping. The CSCO-950 exhibits a low open porosity of $0.6 \pm 0.2\%$, while there are hardly any open pores in CSO-1400 (0% open porosity). The addition of CuO into CSO did not significantly affect the thermal expansion co-efficient ($12.83 \times 10^{-6}\,K^{-1}$ for CSO-1400 and $12.72 \times 10^{-6}\,K^{-1}$ for CSCO-950).

3.5.2. Mechanical strength comparison and fracture mechanism

The biaxial flexural strength (BSF) of CSCO-950 is as high as 257.5 ± 27.4 MPa, which is much higher than that of CSO-1400 (194.4 ± 57.0 MPa). It appears that the doping with this small amount of CuO has a significant effect on both densification and on subsequent strength. On the contrary, Dudek et al.[29] reported that doping of CSO with 5% Y to form $Ce_{0.8}Sm_{0.15}Y_{0.05}O_{2-\delta}$ degraded the bending strength. Zhang et al.[30] found that the addition of over 10% $AlO_{1.5}$ into $Ce_{0.8}Gd_{0.2}O_{2-\delta}$ resulted in an increase in both toughness and hardness, but degraded the conductivity due to the formation of $GdAlO_3$.

SEM analysis was performed to examine the surface and fracture surface of CSO-1400 and CSCO-950 after the flexure strength test (Fig. 9). From Fig. 9a and b, it is noted that CSCO-
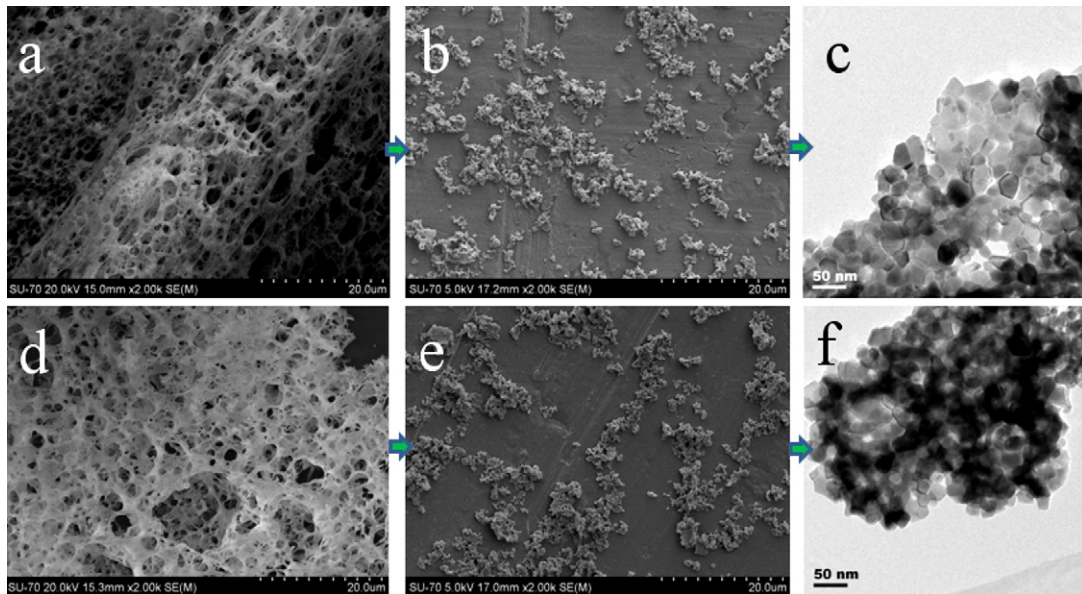
Fig. 7. Micrographs of the CSO and CSCO powders after calcination at 600 °C for 2 h before and after ball-milling: (a) SEM image for foamy CSO before ball-milling; (b) SEM image for micron-sized CSO particles after ball-milling; (c) TEM image for ball-milled CSO; (d) SEM image for foamy CSCO before ball-milling; (e) SEM image for micron-sized CSCO particles after ball-milling; (f) TEM image for ball-milled CSCO.

950 exhibits a dense microstructure of fine-grains (337 ± 18 nm) without obvious grain coarsening, while CSO-1400 is composed of larger grains (959 ± 41 nm). From Fig. 9c and d, it is clear that CSCO-950 has a denser microstructure than CSO-1400 and some spherical closed pores with varied sizes can be identified (Fig. 9c), which originated during sintering. This observation is consistent with the density result in Fig. 8. On the other hand, from the higher magnification fracture images (Fig. 9e and f), for both CSO-1400 and CSCO-950, the microstructures are composed of smooth (black arrow) and rough (black square frames) fracture surfaces, indicating that both intergranular and transgranular fractures are prevalent under biaxial flexural loading. Compared with CSO-1400, CSCO-950 exhibits a much rougher fracture surface, (see black square frames in Fig. 9f), indicating predominantly transgranular mode of fracture. Flexural energy

per unit volume (FEPV) was calculated based on the area of load-deflection curves after the flexure test. The FEPV of CSCO-950 is 74.8 ± 17.1 KJ m^{-3}, which is higher than that of CSO-1400 (53.7 ± 22.0 KJ m^{-3}). It is concluded that during the flexure test, enhanced mechanical strength mainly resulted from higher relative density (less porosity) and a fine-grained microstructure. Moreover, the presence of the small amount of CuO in CSCO which may be segregated at the grain boundaries caused an increase in bond strength and led to transgranular-dominant fracture requiring more energy for crack propagation.

Nevertheless, CSCO-950 exhibits a similar microhardness of 10.5 ± 0.5 GPa to that of CSO-1400 (10.7 ± 0.6 GPa), which can be ascribed to the presence of some open pores ($0.6 \pm 0.2\%$, see Table 1) near the sample surface.

3.5.3. Electrical conductivity comparison

Fig. 10 shows (a) the Arrhenius plots of $\ln(\sigma T)$ versus $1000/T$ and (b) typical impedance spectra measured at 600 °C for CSO-1400 and CSCO-950. The activation energy was calculated from the following Arrhenius equation:

$$\sigma = \left(\frac{\sigma_0}{T}\right) \exp\left(\frac{-Ea}{kT}\right) \qquad (6)$$

where σ, σ_0, Ea, k and T are conductivity, pre-exponential factor, activation energy, Boltzmann constant ($k = 1.38 \times 10^{-23}$ J/K) and absolute temperature, respectively. The activation energy values of CSO-1400 and CSCO-950 are 0.99 eV and 0.73 eV, which were calculated from the slopes of the plots in Fig. 10a. The activation energy of CSO-1400 is very close to that of the carbonate-coprecipitation processed Ce$_{0.8}$Sm$_{0.2}$O$_{1.9}$ ($\sim$1.0 eV) sintered at the same temperature,[31] but it is higher than that of the solid-state reacted CSO (0.82 eV)[32] and the hydrothermal derived CSO (0.87 eV).[33] The difference in activation energy for CSO can be ascribed to many factors, such as purity of
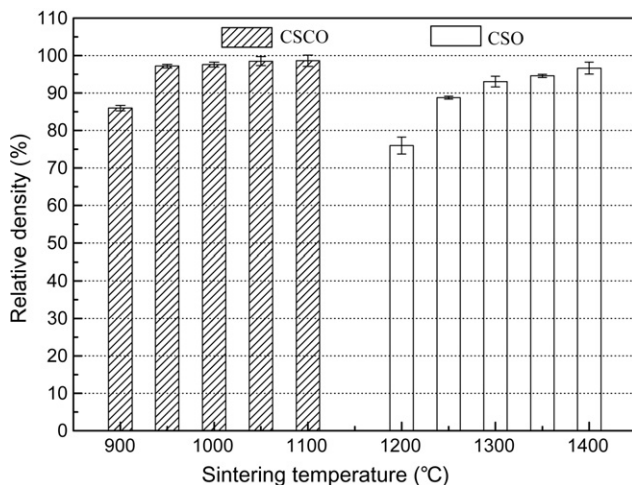

Fig. 8. Relative densities of the sintered CSCO and CSO compacts as a function of sintering temperature.
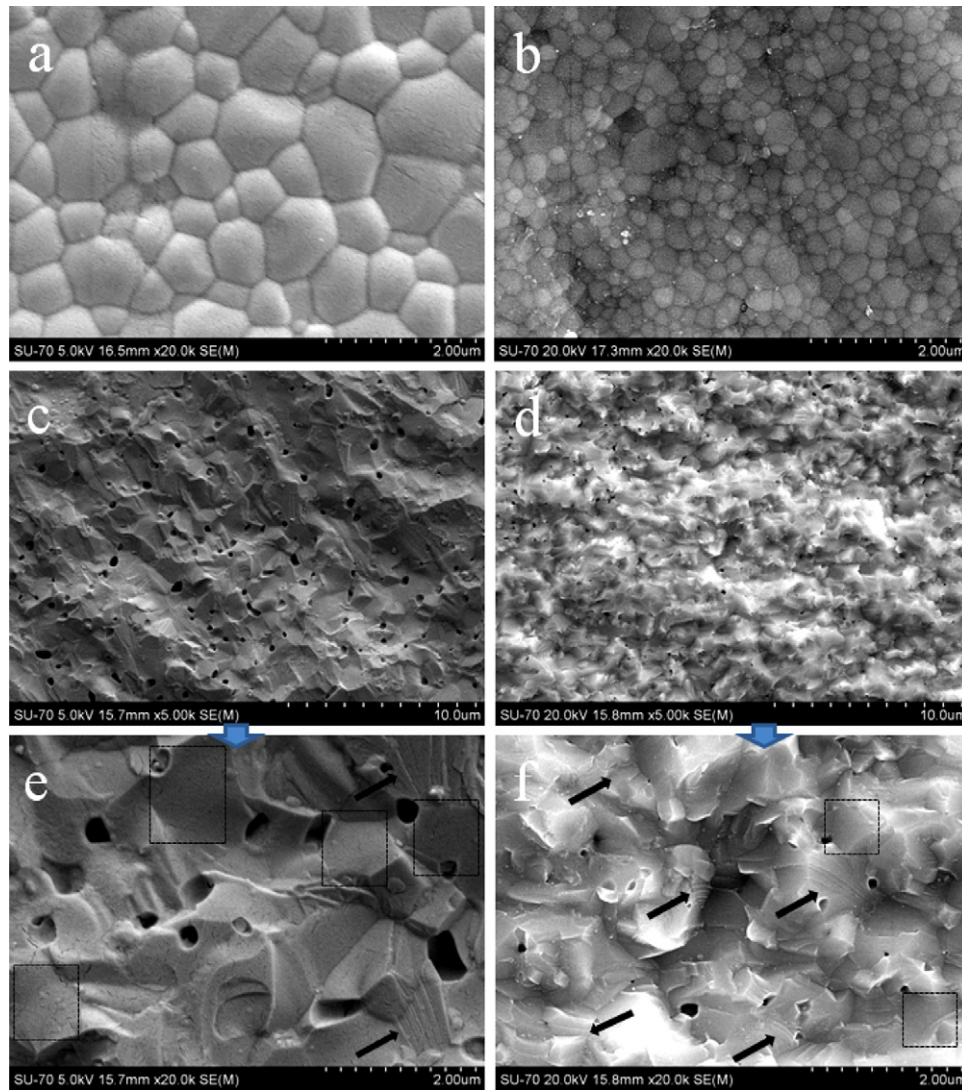
Fig. 9. SEM micrographs of the surfaces and fracture surfaces (after flexural strength test) of sintered CSO and CSCO: (a) surface of the CSO sintered at 1400 °C; (b) surface of the CSCO sintered at 950 °C. (c) low magnification fracture surface of the CSO sintered at 1400 °C; (d) low magnification fracture surface of the CSCO sintered at 950 °C; (e) high magnification fracture surface of the CSO sintered at 1400 °C; (f) high magnification fracture surface of the CSCO sintered at 950 °C.

starting materials, microstructure parameters of sintered bodies. Nevertheless, the addition of 1 mol% Cu into CSO could decrease activation energy and therefore increase total electrical conductivity.

The CSO-1400 has total conductivities of 0.00652 S cm^{-1} at 600 °C and 0.02032 S cm^{-1} at 700 °C, which is slightly higher than that (0.017 S cm^{-1} at 700 °C) of PVA-processed CSO reported by Ma et al.[20] In contrast, the CSCO-950 exhibits significantly improved total conductivities of 0.0154 S cm^{-1} at 600 °C and 0.0369 S cm^{-1} at 700 °C. Considering identical relative densities between CSO-1400 and CSCO-950, this improvement of conductivity can be ascribed to the microstructure of CSCO-950 which has the advantage of increasing the number of grain boundaries, thus allowing the dopants to be more widely dispersed with reduced concentrations at each grain interface and facilitating the movement of oxygen vacancies across grain boundaries.[34] As shown in Fig. 10b, CSO-1400

and CSCO-950 exhibit quite different impedance spectra characteristics at 600 °C. In addition to the electrode polarization behaviour (EPB), the impedance spectrum of CSO-1400 also shows the effects of grain boundaries. In summary, the addition of a minor amount of Cu is a quite effective method to prepare a doped CSO electrolyte with enhanced electrical conductivity.

Fig. 11 shows the Raman spectra of CSO-1400 and CSCO-950, which both show two distinctive bands, at around 460 cm^{-1} and 570 cm^{-1}. The band at 460 cm^{-1} can be assigned to a symmetric breathing mode of oxygen atoms around cerium ions. The additional weak band at around 570 cm^{-1} is attributed to the oxygen vacancies formed by doping with aliovalent elements. When Sm^{3+} or Cu^{2+} are substituted for Ce^{4+} ions, oxygen vacancies are introduced to maintain electrical neutrality, which will yield a broad peak on the high frequency side of the F$_{2g}$ band. When 1 at.% Cu^{2+} was co-doped into CSO and substituted for Ce^{4+}, the intensity of the peak around 570 cm^{-1} increases slightly,
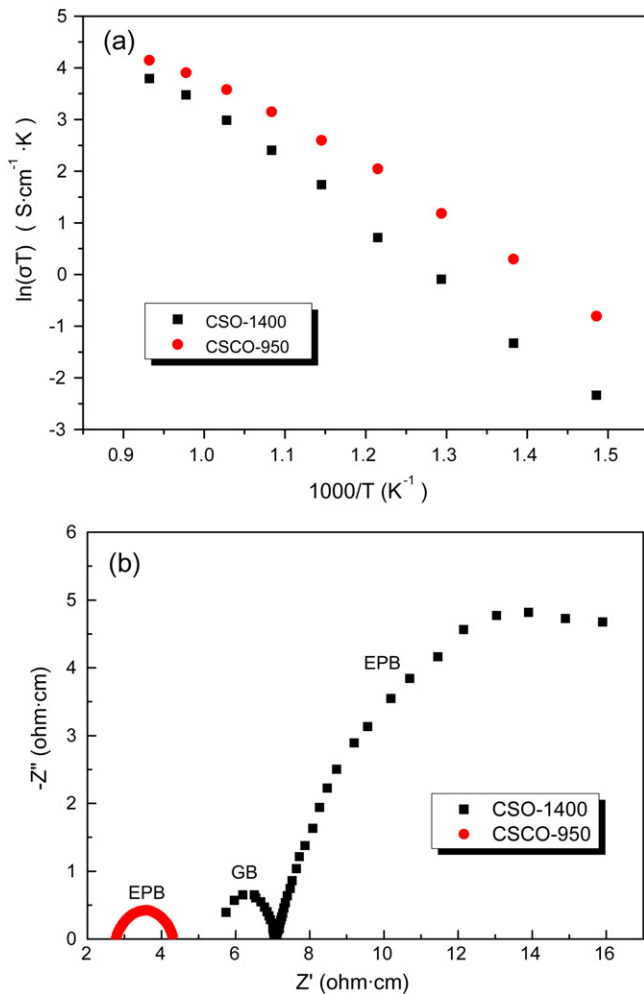
Fig. 10. The electrical conductivity results for the CSO sintered at 1400 °C and CSCO sintered at 950 °C: (a) Arrhenius plots of $\ln(\sigma T)$ versus $1000/T$; (b) AC impedance spectra of the CSO sintered at 1400 °C and CSCO sintered at 950 °C, measured at 600 °C.
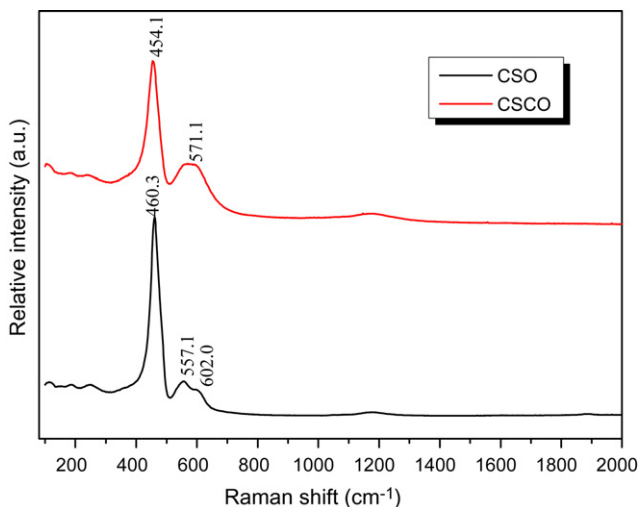

Fig. 11. Raman spectra of the CSO sintered at 1400 °C and CSCO sintered at 950 °C.

indicating the oxygen vacancy concentration in CSCO-950 is higher than that in CSO-1400. This is consistent with the results for 2 at.% Pr-doped CSO obtained by Liu et al.[35] and explains the increase observed in electrical conductivity.

4. Conclusions

In this work, nano-sized CSO and CSCO were both synthesized by the PVA assisted combustion method, and then characterized in terms of the structure of PVA–cation complexes and formation behaviour of nano-powders, and the mechanical and electrical performance of sintered bodies. The following conclusions can be drawn:

(1) During PVA chelation, the PVA–cation complexes were formed by coordinating metal cations to hydroxyl groups, as well as the COO^{-1} group derived from the oxidation of PVA with NO_3^{-1}. This resulted in a homogeneous distribution of metal cations at an atomic scale in the network of PVA-based sol and dried gel.
(2) For both CSO and CSCO, low temperatures (around 200 °C) caused the occurrence of intense combustion reactions, during which combustion heat was released and the removal of organic substances, resulting in the crystallization of CSO (10–20 nm) and CSCO (10–15 nm) nano-crystals with cubic fluorite structure. Direct solid solution of Sm_2O_3 and CuO occurs into the lattice of CeO_2. All metal elements distribute quite homogeneously in the combustion processed CSCO.
(3) The slight compositional modification of CSO by co-doping with a small amount of CuO (1 at.%) resulted in a significantly reduced sintering temperature (950 °C), enhanced mechanical strength and electrical conductivity. The improvement in strength can be ascribed to the dense and fine-grained microstructure (grain size: 337 ± 18 nm) of CSCO-950, due to its transgranular-dominant fracture mode during the flexural strength test, while CSO-1400 exhibited a submicron-grained microstructure (0.959 ± 0.041 μm) with slightly lower relative density. Furthermore, the addition of 1 mol% Cu resulted in an improvement in electrical conductivity with lower activation energy due to high oxygen vacancy concentration.

References

1. Steele BCH, Heinze A. Materials for fuel-cell technologies. *Nature* 2001;**414**:345–52.
2. Yamashita K, Ramanujachary KV, Greenblatt M. Hydrothermal synthesis and low temperature conduction properties of substituted ceria ceramics. *Solid State Ionics* 1995;**81**:53–60.

3. Lin B, Sun WP, Xie K, Dong YC, Dong DH, Meng GY, et al. A cathode-supported SOFC with thin $Ce_{0.80}Sm_{0.2}O_{1.9}$ electrolyte prepared by a suspension spray. *J Alloys Compd* 2008;**465**:285–90.

4. Gil V, Tartaj J, Moure C, Duran P. Sintering, microstructural development, and electrical properties of gadolinia-doped ceria electrolyte with bismuth oxide as a sintering aid. *J Eur Ceram Soc* 2006;**26**:3161–71.

5. Kleinlogel C, Gauckler LJ. Sintering and properties of nanosized ceria solid solutions. *Solid State Ionics* 2000;**135**:567–73.

6. Yu T, Joo J, Park YI, Hyeon T. Large-scale nonhydrolytic sol–gel synthesis of uniform-sized ceria nanocrystals with spherical, wire, and tadpole shape. *Angew Chem* 2005;**117**:7577.

7. Rocha RA, Muccillo ENS. Effect of calcination temperature and dopant content on the physical properties of ceria-gadolinia prepared by the cation complexation technique. *Cerâmica* 2001;**47**:219–24.

8. Zhang TS, Ma J, Kong LB, Hing P, Leng YJ, Chan SH, et al. Sinterability and ionic conductivity of coprecipitated $Ce_{0.8}Gd_{0.2}O_{2-\delta}$ powders treated via a high-energy ball-milling process. *J Power Sources* 2003;**124**:26–33.

9. Aruna ST, Mukasyan AS. Combustion synthesis and nanomaterials. *Curr Opin Solid State Mater Sci* 2008;**12**:44–50.

10. Rozenberg BA, Tenne R. Polymer-assisted fabrication of nanoparticles and nanocomposites. *Prog Polym Sci* 2008;**33**:40–112.

11. Jiu JT, Ge Y, Li XN, Nie L. Preparation of Co_3O_4 nanoparticles by a polymer combustion route. *Mater Lett* 2002;**54**:260–3.

12. Yang W, Qi YL, Ma YJ, Li XE, Guo XJ, Gao JZ, et al. Synthesis of Nd_2O_3 nanopowders by sol–gel auto-combustion and their catalytic esterification activity. *Mater Chem Phys* 2004;**84**:52–7.

13. Lee SJ, Kriven WM. Crystallization and densification of nano-size amorphous cordierite powder prepared by a PVA solution-polymerization route. *J Am Ceram Soc* 1998;**81**:2605–12.

14. Lee SJ, Shin PW, Kim JW, Chun SY. Characteristics of porous YAG powders fabricated by PVA polymer solution technique. *Mater Sci Forum* 2007;**534-36**(1):21–4.

15. Gulgun MA, Nguyen MH, Kriven WM. Polymerized organic–inorganic synthesis of mixed oxides. *J Am Ceram Soc* 1999;**82**:556–60.

16. Song JT, Young JF. Direct synthesis and hydration of calcium aluminosulfate ($Ca_4Al_6O_{16}S$). *J Am Ceram Soc* 2002;**85**:535–9.

17. Subramania A, Angayarkanni N, Vasudevan T. Effect of PVA with various combustion fuels in sol–gel thermolysis process for the synthesis of $LiMn_2O_4$ nanoparticles for Li-ion batteries. *Mater Chem Phys* 2007;**102**:19–23.

18. Rocha RA, Muccillo ENS. Preparation of nanocrystalline gadolinia doped ceria powders by combustion synthesis process. *Br Ceram Trans* 2003;**102**:216–8.

19. Ray JC, Saha CR, Pramanik P. Stabilized nanoparticles of metastable ZrO_2 with Cr^{3+}/Cr^{4+} cations: preparation from a polymer precursor and the study of the thermal and structural properties. *J Eur Ceram Soc* 2002;**22**:851–62.

20. Ma JJ, Jiang CR, Zhou XL, Meng GY, Liu XQ. Polyvinyl alcohol-induced low temperature synthesis of CeO_2-based powders. *J Power Sources* 2006;**162**:1082–7.

21. Gorbova E, Maragou V, Medvedev D, Demin A, Tsiakaras P. Influence of Cu on the properties of gadolinium-doped barium cerate. *J Power Sources* 2008;**181**:292–6.

22. Kang YJ, Choi GM. The effect of alumina and Cu addition on the electrical properties and the SOFC performance of Gd-doped CeO_2 electrolyte. *Solid State Ionics* 2009;**180**:886.

23. Park JS, Lee JH, Lee HW, Kim BK. Low temperature sintering of $BaZrO_3$-based proton conductors for intermediate temperature solid oxide fuel cells. *Solid State Ionics* 2010;**181**:163–7.

24. Dong YC, Hampshire S, Lin B, Ling YH, Zhang XZ. High sintering activity Cu–Gd co-doped CeO_2 electrolyte for solid oxide fuel cells. *J Power Sources* 2010;**195**:6510–5.

25. Timoschenko S, Woinowsky-Kreiger S. *Symmetrical bending of circular plates, theory of plates and shells*. 2nd ed. New York: McGraw-Hill; 1959. p. 106–7.

26. Curran DJ, Fleming TJ, Towler MR, Hampshire S. Mechanical properties of hydroxyapatite-zirconia compacts sintered by two different sintering methods. *J Mater Sci Mater Med* 2010;**21**:1109–20.

27. Wang JC, Liu QF, Liu Q. Ceria- and Cu-doped ceria nanocrystals synthesized by the hydrothermal methods. *J Am Ceram Soc* 2008;**91**:2706–8.

28. Shannon RD. Revised effective ionic radii in halides and chalcogenides. *Acta Crystallogr* 1976;**A32**:751–67.

29. Dudek M, Bogusz W, Zych Ł, Trybalska B. Electrical and mechanical properties of CeO_2-based electrolytes in the CeO_2–Sm_2O_3–M_2O_3 (M = La, Y) system. *Solid State Ionics* 2008;**179**:164–7.

30. Zhang TS, Zeng ZQ, Huang HT, Hing P, Kilner J. Effect of alumina addition on the electrical and mechanical properties of $Ce_{0.8}Gd_{0.2}O_{2-\delta}$ d ceramics. *Mater Lett* 2002;**57**:124–9.

31. Li HB, Xia CR, Zhu MH, Zhou ZX, Meng GY. Reactive $Ce_{0.8}Sm_{0.2}O_{1.9}$ powder synthesized by carbonate coprecipitation: Sintering and electrical characteristics. *Acta Mater* 2006;**54**:721–7.

32. Dirstine RT, Blumenthal RN, Kuech TF. Ionic conductivity of calcia, yttria, and rare earth-doped cerium dioxide. *J Electrochem Soc* 1979;**126**(2):264–9.

33. Huang W, Shuk P, Greenblatt M. Hydrothermal synthesis and properties of $Ce_{1-x}Sm_xO_{2-x/2}$ and $Ce_{1-x}Ca_xO_{2-x}$ solid solutions. *Chem Mater* 1997;**9**:2240–5.

34. Chen M, Kim BH, Xu Q, Ahn BK, Kang WJ, Huang DP. Synthesis and electrical properties of $Ce_{0.8}Sm_{0.2}O_{1.9}$ ceramics for IT-SOFC electrolytes by urea-combustion technique. *Ceram Int* 2009;**35**:1335–43.

35. Ji Y, Liu J, He TM, Wang JX, Su WH. The effect of Pr co-dopant on the performance of solid oxide fuel cells with Sm-doped ceria electrolyte. *J Alloys Compd* 2008;**465**:285–90.